Coupling atomization, emulsification, and polymerization steps for creating gel microspheres

S. Danial Naghib, Matin Mirbaha, Kristina Logushkova, Jérôme Bibette, and Nicolas Bremond*

Laboratoire Colloïdes et Matériaux Divisés, CBI, ESPCI Paris, Université PSL, CNRS, 10 rue Vauquelin, F-75005 Paris, France

(Received 11 March 2024; accepted 24 July 2024; published 15 August 2024)

Calibrated gel microspheres are used in several life-science applications, from embolization to DNA barcoding and drug delivery. Along with selecting or designing specific materials that depend on the application, various processes have been developed to produce such hydrogel particles. Here, we report a high throughput strategy that is based on the controlled fragmentation of an aqueous jet in air that results in droplets of monomer solution, their entry and collection in an oil bath, followed by polymerization of the emulsion droplets which thus turn into gel beads. Each step of the process is detailed and the operating conditions are optimized to obtain homogeneous polyacrylamide gel microspheres. The impact area of the stream of droplets at the free surface, that can be tuned with the help of an electric field, plays a major role in minimizing coalescence of droplets as well as mass transport between the dispersed phase and the continuous phase which is correlated to the sedimentation flow features of the dilute emulsion.

DOI: 10.1103/PhysRevFluids.9.083604

I. INTRODUCTION

Hydrogels are percolated networks of hydrophilic macromolecules that are physically or chemically cross-linked and highly swollen by water [1]. Often encountered in nature, from plants [2] to mammals [3], biocompatible hydrogels have been designed for biomedical applications like tissue engineering [4] or drug delivery [5]. Hydrogels can also be used in sensors, actuators, and various devices [6] but also in various other fields once additional materials are incorporated into the matrix, like conductive particles for energy storage, for example [7]. Also, fine tuning supramolecular interactions with specific and directional dynamic bonds offers new functionalities like self-healing or stimuli-responsiveness [8,9].

Concomitantly to the choice of polymer properties or cross-link type, processes for shaping hydrogels are also a crucial aspect for the final application. More specifically, hydrogel shaped as microspheres are well suited for biomedical applications [10]. In addition, controlling size homogeneity and mechanical properties offers unique tools for single cell studied [11], like DNA barcoding in droplets for single cell analysis [12], but also as calibration beads for mechanical analysis of cells [13], or for embolization [14].

Gel microspheres are usually obtained from droplet templating of monomers mixed with initiators, dispersed in an immiscible phase containing a catalyzer for free radical polylmerization, a process referred as inverse suspension polymerization [15]. To control gel bead size, microfluidic technology is the most suited approach as it offers efficient emulsification processes leading to well calibrated emulsion droplets [16,17] and thus gel microspheres [18,19]. While microfluidics is a

*Contact author: nicolas.bremond@espci.fr

 ©2024 American Physical Society

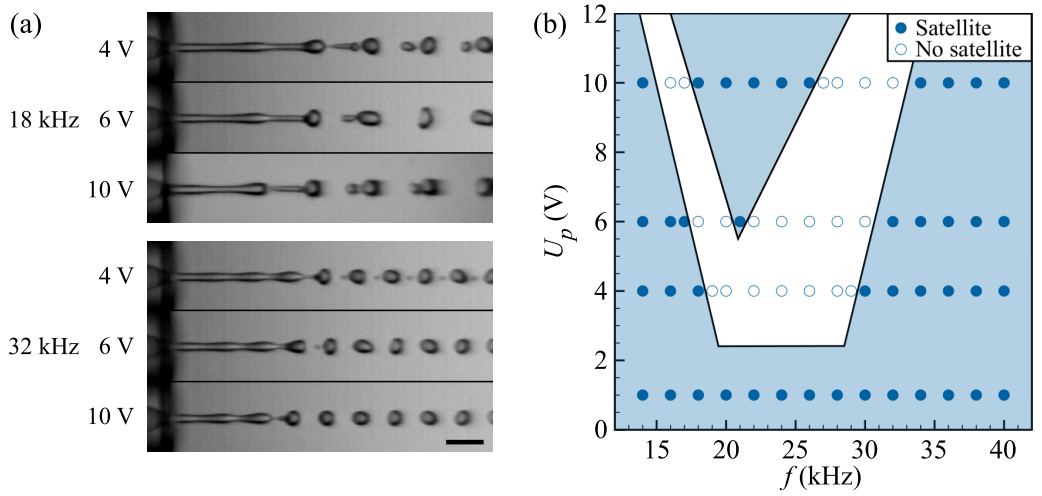

FIG. 1. (a) Snapshots of a water jet under harmonic perturbation with various frequencies f and amplitude U_p of the piezoelectric element. The injector diameter d_i is 40 μm and the flow rate is 30 ml/h. Scale bar is 200 μm. (b) Corresponding mapping of the presence or not of satellite droplets in the $\{f, U_p\}$ plane.

very powerful tool to control droplet size and thus bead size, increasing the rate of production is often a challenge. Here, we propose a strategy that couples a controlled atomization step of a liquid jet, which is well suited to produce droplets in air at a high throughput, and an inverse suspension polymerization of the droplets collected in an oil bath. In the following, we detail each step of the process, namely atomization, emulsification and polymerization, and give optimal conditions to obtain well calibrated gel microspheres.

II. RESULTS AND DISCUSSION

A. Atomization

Water droplets containing monomers are first created in air *via* the controlled fragmentation of a liquid jet. Such control is obtained by using ink-jet technology in a continuous mode. To be more precise, liquid is flowing through a glass capillary, surrounded by a piezoelectric element, that ends with a contraction of the inner diameter until a size d_i. A jet is formed above a critical flow rate q that depends on d_i and fluid properties and can be expressed through a critical Weber number defined as $\mathrm{We} = \rho d_i u_i^2/\gamma$, where $u_i = 4q/(\pi d_i^2)$ is the average velocity at the exit, ρ the liquid density and γ its surface tension [20]. Since the injector diameter d_i varies between 25 μm and 50 μm, the corresponding Bond number $\mathrm{Bo} = \rho g d_i^2/\gamma$ is of the order of 10^{-4}. Therefore, the gravity does not influence jet formation. Also, the viscosity of the aqueous solutions being close to water's viscosity, the Ohnesorge number $\mathrm{Oh} = \nu(\rho/d_i\gamma)^{1/2}$ is of the order of 2×10^{-2} and viscosity does not affect jet formation neither. Dripping to jetting transition is thus solely driven by inertia and the critical We is equal to 4 [21]. Accordingly, this threshold corresponds to a minimal flow rate spanning from 6 to 17 ml/h in the present study.

For a given flow rate, one would expect that the droplet diameter d is simply linked to the frequency f of the sinusoidal voltage applied to the piezoelectric element, i.e., $q = \pi d^3 f/6$. However, because of the asymmetric nature of jet pinch-off profile, a satellite droplet is formed [22], thus leading to a bimodal droplet size distribution [Fig. 1(a)]. The size of the satellite droplet is an increasing function of the selected wavelength λ of the capillary instability and thus a decreasing function of f since $\lambda = u_j/f$ where $u_j = u_i(d_i/d_j)^2$ is the velocity in the jet. The jet size d_j is deduced from the conservation of momentum and mass between the flow inside the injector and in

the jet where flow profile has relaxed to a plug one [23]. For large value of the Reynolds number $\mathrm{Re} = u_i d_i/\nu$, which is here larger than 10^2, d_j is expressed as a function of the Weber number $d_j/d_i = \sqrt{3}/2(1 + 1/(10\mathrm{We}))$ [24]. In the present experiments, the Weber number is larger than 10 and the jet size d_j is simply

$$d_j = \frac{\sqrt{3}}{2} d_i, \tag{1}$$

thus about $0.87 \times d_i$ [25] and the jet velocity is

$$u_j = \tfrac{4}{3} u_i. \tag{2}$$

Since the breakup of the two liquid bridges that link the future satellite droplet to the two neighboring main droplets do not occur simultaneously, the satellite droplet acquires a velocity different than the main droplets one. This velocity contrast then leads to droplet collision and might end up in droplet merging [26], as observed in Fig. 1(a) for $f = 18\,\mathrm{kHz}$ and $U_p = 10\,\mathrm{V}$, or for $f = 32\,\mathrm{kHz}$ and $U_p = 6\,\mathrm{V}$. However, as discussed later on, the use of an electric field to spread droplets in the lateral direction prevent droplets to coalesce. Fortunately, the formation of satellite droplets can be suppressed for certain ranges of frequency and amplitude of the piezoelectric actuator as shown Fig. 1(a) for $f = 18\,\mathrm{kHz}$ and $U_p = 6\,\mathrm{V}$ and for $f = 32\,\mathrm{kHz}$ and $U_p = 10\,\mathrm{V}$. Such a formation is hindered when the liquid bridge linked to the rear main droplet breaks much before the front one, thus leading to a fast recoiling of the free surface after pinch-off towards the front main droplet. This large dissymmetry might be due to nonlinear pressure or velocity fields induced by the piezoelectric element [27]. The existence or not of satellite droplets is mapped as a function of f and U_p for a given flow rate and injector diameter as shown in Fig. 1(b). At low voltage, equal here to 1 V, satellite droplet is always present whatever the frequency. A region where an unimodal droplet size distribution is obtained exists for larger values of U_p and specific ranges of frequency. Therefore, for a given flow rate, droplet size is controlled by both adjusting the frequency and the voltage of the electrical signal sent to the piezoelectric element.

Right after jet breakup, the droplet velocity, deduced from mass and momentum conservation [22,28], is

$$u_{d0} = u_j \left(1 - \frac{u_c^2}{u_j^2}\right), \tag{3}$$

where

$$u_c = \sqrt{\frac{2\gamma}{\rho d_j}} \tag{4}$$

is the receding speed of a liquid cylinder's free edge driven by surface tension in the inviscid limit. By using Eqs. (1) and (2), droplet velocity can then be expressed as a function of the average velocity in the injector u_i and the Weber number, i.e.,

$$u_{d0} = \frac{4}{3}\left(1 - \frac{3\sqrt{3}}{4\mathrm{We}}\right) u_i, \tag{5}$$

which is larger than 6 m/s in the present experiments.

B. Emulsification

We now discuss the fate of droplets from their formation in air to their entry into the oil pool and where the main objective is to conserve droplet size homogeneity, thus avoiding fragmentation or coalescence during the transition from a spray to an emulsion at the free surface. The controlled jet breakup step leads to the formation of a regular train of droplets [Fig. 2(a)]. The initial distance

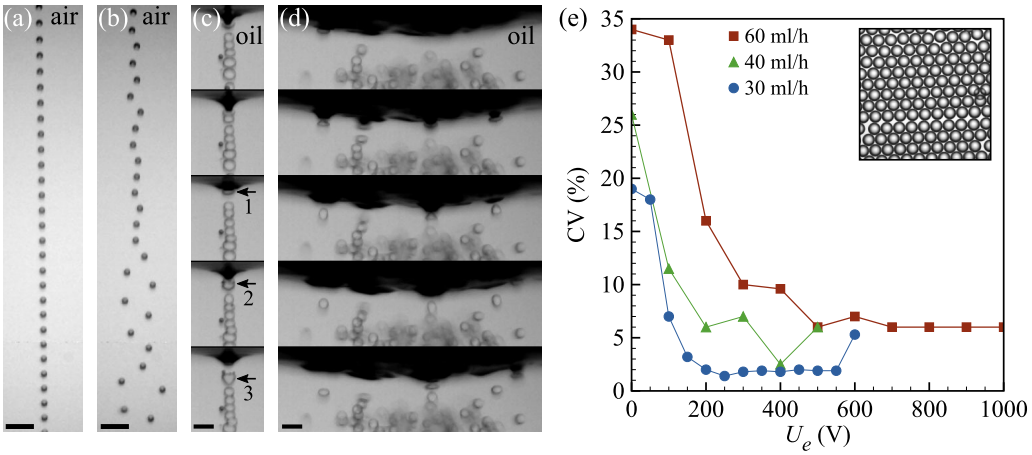

FIG. 2. Regular stream of droplets in air (a) without and (b) with an electric field, scale bar is 500 μm. Time sequences showing the formation of water-in-oil emulsion when water droplets enter into the oil bath (c) without and (d) with an electric field, scale bar is 200 μm and time step is 50 μs. Arrows indicate a droplet coalescence event. (e) Coefficient of variation of the emulsion droplet size as a function of the electrode voltage U_e for different flow rates with $d_i = 50$ μm. The frequency is adjusted for each flow rate to keep the droplet size constant and equal to 100 μm. Inset: microscope image of monodisperse emulsion with CV around 2%.

between the droplets λ_{d0} depends on droplet velocity u_{d0} after break-up and the applied frequency f, i.e., $\lambda_{d0} = u_{d0}/f$. If water evaporation is neglected, then mass conservation implies that the frequency is constant since $q = m_d f/\rho$, where m_d is the mass of a droplet. As discussed later on, the velocity of the droplets decreases during their flight towards the oil bath because of air drag. Ideally, they all experience the same deceleration and λ_{d0} is homogeneously decreasing. However, if there exists small fluctuations of u_{d0}, due to slight variations of the flow rate, for example, then droplets would come closer to each other mainly because of kinematic gathering which is enhanced by air drag that depends on droplet velocity. If droplets do not touch each other prior to reaching the oil bath, then they experience, one after the other, a strong deceleration when entering the oil bath which has a higher viscosity than air and thus lead to stronger drag force. As a consequence, the droplets collide and form a compact train of droplets as shown in Fig. 2(c). A coalescence event is also observed where a first droplet, indicated by an arrow and labeled 1, is hit by a second droplet (label 2) which finally coalesce with the first droplet (label 3). Adsorption kinetics of surfactants at the oil-water interface is thus not efficient enough to prevent collision-induced merging when droplets cross the oil-free surface.

To overcome this issue, a standard approach is to use an electric field such that droplets acquire a net electric charge and repulse each other [Fig. 2(b)], thus forming a cone spray [29,30]. As a consequence, the impact area is increased and the probability of droplet collision at the free surface is reduced [Fig. 2(d)]. The coefficient of variation (CV) of the droplet size, defined as the ratio between the standard deviation and the mean of the size distribution, is reported in Fig. 2(e) as a function of the electrode potential U_e for three different flow rates. Here, the mean drop size is kept constant and equal to 100 μm by adjusting the frequency of actuation for each flow rate. The flow rate being equal to 30, 40, and 60 ml/h, the frequency is then set to 16, 21, and 32 kHz, respectively. For the lowest flow rate, we notice that for U_e above 200 V the CV drops down to about 2%, corresponding to a monodisperse emulsion. For the intermediate flow rate, the CV reaches also such a low value but at a higher voltage, equal to 400 V. A further increase of the flow rate leads to broader size distributions with a minimal CV close to 6%. Since drop size variation is linked to drop-drop impact that can result in a coalescence event, the spray features is then discussed.

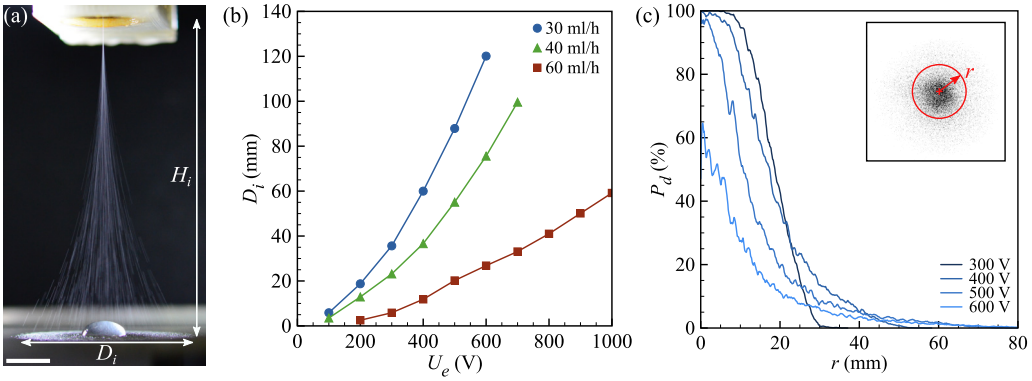

FIG. 3. (a) Long time exposure snapshot of the conical spray formed when the water jet is surrounded by a cylindrical electrode set at a voltage U_e. The droplets impact on a grounded plate placed at a distance $H_i = 8$ cm from the electrode and where an impact diameter D_i can be measured. Scale bar is 1 cm. (b) Evolution of the impact diameter as a function of U_e for the same q, d and d_i in Fig. 2(e). (c) Probability P_d to find a drop at a distance r from the jet axis in a plane located at $H_i = 15$ cm for $q = 50$ ml/h, $d = 100$ μm and various U_e. Inset: Example of the impact of inked drops on a paper sheet from which P_d is determined.

A characteristic spray shape is shown in Fig. 3(a) from which an impact diameter D_i of droplets collected on grounded metallic plate can be measured. It is defined as the maximal lateral displacement of droplets at a distance H_i from the end of the electrode and the grounded plate. As reported in Fig. 3(b), D_i is an increasing function of the applied voltage at the electrode and a decreasing function of the flow rate. We note that the minimal CV for q equal to 30 and 40 ml/h is obtained for D_i equal or larger than 40 mm. However, for 60 ml/h, such a low CV is not obtained even though the droplets are spread over a region larger than 40 mm. Collision of droplets while they are crossing the free surface can thus not be avoided for this higher flux of droplets. Snapshots of the spray as the one shown in Fig. 3(a) only give access to the envelop of the spray. To evaluate how droplets are distributed inside the spray, inked droplets are collected for a few seconds on a paper sheet placed above the grounded plate. A typical realization is reported in the inset of Fig. 3(c). From such an image, the probability P_d to encounter a droplet at a distance r from the center of the impact pattern can be measured. This probability is plotted in Fig. 3(c) for various values of the electrode voltage U_e.

These features are correlated to the net charge acquired by each droplet. Due to the presence of ionic species, water can be considered as a conductor. The surface charge of the liquid jet formed inside the cylindrical electrode can be modeled as a coaxial capacitor. Assuming that the charge q_e carried by a droplet corresponds to the surface charge of a cylinder having a length $\lambda = u_j/f$, q_e is given by [28]

$$q_e = \frac{2\pi\varepsilon_0\lambda U_e}{\ln(d_e/d_j)}, \tag{6}$$

where ε_0 is the permittivity of vacuum and d_e the inner electrode diameter. If the droplet train is regularly spaced and well aligned, then all droplets are subjected to the same electrostatic repulsive force arising from their neighbors. However, a slight lateral deviation of droplet's center of mass leads to a net lateral force which induces a widening of the initially aligned stream of droplets (Fig. 4). We note that this lateral spreading occurs for large enough electrical charge which otherwise smooths out any fluctuations of inter-droplet distance [31]. The electrostatic force experienced by a droplet at a location $\mathbf{r}$ surrounded by two droplets located at $\mathbf{r}_1$ and $\mathbf{r}_2$ is

$$\mathbf{F}_e = \frac{q_e^2}{4\pi\varepsilon_0}\left(\frac{\mathbf{r}-\mathbf{r}_1}{|\,\mathbf{r}-\mathbf{r}_1\,|^3} + \frac{\mathbf{r}-\mathbf{r}_2}{|\,\mathbf{r}-\mathbf{r}_2\,|^3}\right). \tag{7}$$

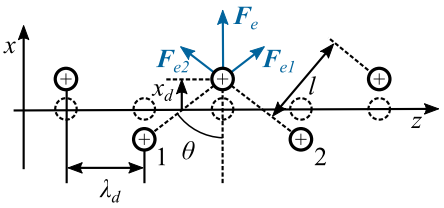

FIG. 4. Schematics of the droplet train destabilization with the most amplified wavelength, equal to $2\lambda_d$, and the resulting lateral force exerted by the two closest neighboring droplets.

For small lateral deviation x_d compared to the distance between droplets, a perturbation analysis leads to an exponential growth of the lateral motion [32]

$$x_d(t) = x_{d0} e^{\sigma t + i k_t n \lambda_d}, \tag{8}$$

where x_{d0} is the initial amplitude of the lateral displacement, σ is the growth rate associated to the wave number $k_t = 2\pi/\lambda_t$ with λ_t the wavelength of the perturbation which a multiple number n of the initial distance between two neighboring droplets λ_d. We note that the stability analysis is performed for a two dimensional case that results in a planar spray. However, the spray adopts a conical shape that results from motion of the droplets in the {x,y} plane [Fig. 2(b)]. For the sake of simplicity, we use the two-dimensional description to rationalize our observations as previously done for 500 μm charged drops [33]. The most amplified wavelength is equal to $2\lambda_d$, corresponding to an opposite motion of closest neighboring droplets away from the droplet train axis (Fig. 4), with a growth rate given by

$$\sigma_m = \frac{q_e}{\left(\pi \varepsilon_0 m_d \lambda_d^3\right)^{1/2}}. \tag{9}$$

The lateral displacement is finally given by

$$x_d(t) = x_{d0} e^{\sigma_m t}. \tag{10}$$

A time sequence showing the destabilization of an initially regular train of droplets is reported in Fig. 5. The lateral motion of two droplets marked by a circle and a square is plotted in Fig. 6(a). We note that the exponential growth is a good approximation of the lateral motion up to 200 μm. Then

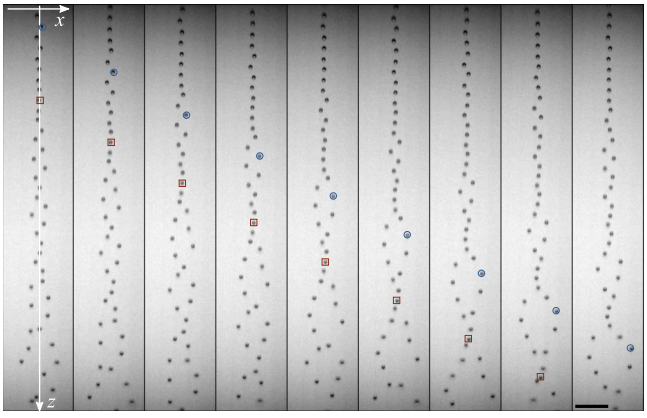

FIG. 5. Time sequence showing the destabilization of a train of charged droplets initially moving along the z axis. Time step between two snapshots is 0.25 ms, scale bar is 1 mm. The injector diameter d_i is 40 μm, the drop size is 100 μm and the flow rate is 32 ml/h.

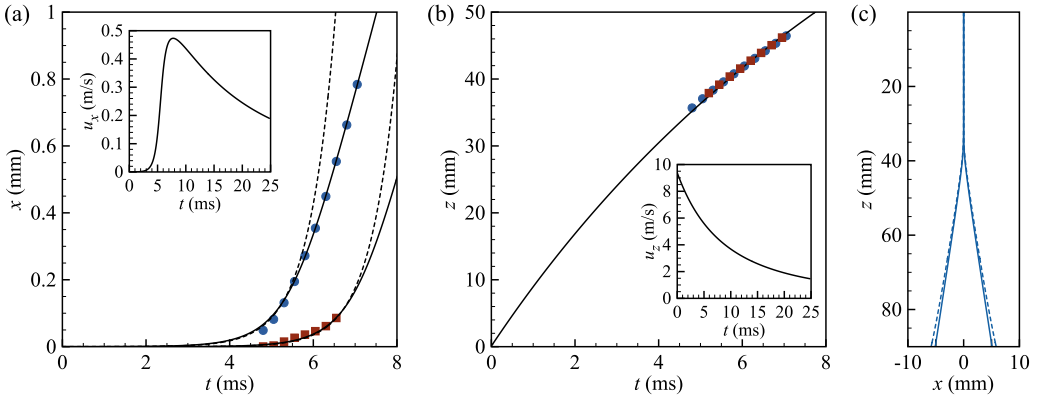

FIG. 6. (a) Time evolution of the lateral displacement x of the droplets marked by a blue circle and a red square in Fig. 5. The dashed line is given by Eq. (10) and the continuous one by Eq. (13). Inset: lateral droplet velocity as a function of time for a longer flight time. (b) Time evolution of the longitudinal displacement z of the droplets marked by a blue circle and a red square in Fig. 5. The continuous line is given by Eq. (14). Inset: longitudinal droplet velocity as a function of time for a longer flight time. (c) Corresponding droplet trajectory obtained from Eqs. (13) and (14) (continuous line) and when the electric field generated by the electrode is taken into account in Eq. (16) (dashed line).

the lateral velocity seems to saturates, because of the vanishing electrostatic force thus leading to a linear displacement. We note here that, to fit the experimental data, the charge of the droplet given by Eq. (6) is reduced by almost a factor 3, probably because the jet was set at the entrance of the electrode for this experiment, leading to a smaller local electric field and thus electric charge. In any event, the decay of the repulsive force needs to be accounted for correctly evaluating the final lateral velocity and thus the impact diameter.

For the case considered here and sketched in Fig. 4, the electrostatic force along x given by Eq. (7) becomes

$$F_e = \frac{q_e^2}{2\pi\varepsilon_0}\frac{\cos\theta}{l^2}, \tag{11}$$

where l is the distance between closest neighboring droplets and θ is the angle defined by $\cos\theta = 2x_d/l$. The lateral force is finally

$$F_e = \frac{q_e^2}{2\pi\varepsilon_0}\frac{x_d}{\left(\lambda_d(z)^2 + x_d^2\right)^{3/2}}, \tag{12}$$

where the distance λ_d is a function of z since it is linked to the velocity $u_{d,z}$ of the drop along the vertical direction, i.e., $\lambda_d = u_{d,z}/f$, which is slowed down because of air drag. The equation of motion of the droplet along the x axis is then written as

$$m_d\frac{d^2x_d}{dt^2} = -\frac{q_e^2}{2\pi\varepsilon_0}\frac{x_d}{\left(\lambda_d(z)^2 + x_d^2\right)^{3/2}} - \frac{\pi}{8}\rho_{\text{air}}d^2C_d u_d^2\sin\alpha, \tag{13}$$

and along z

$$m_d\frac{d^2z_d}{dt^2} = m_d g - \frac{\pi}{8}\rho_{\text{air}}d^2C_d u_d^2\cos\alpha, \tag{14}$$

where u_d is the droplet velocity and α the angle between the droplet velocity vector and the vertical axis, i.e., $\tan\alpha = u_{d,x}/u_{d,z}$. The drag coefficient C_d depends on the droplet Reynolds number $\text{Re}_d = u_d d/\nu_{\text{air}}$. In the case of a solid sphere, for low Reynolds numbers, $\text{Re}_d < 0.5$, the drag force is

purely viscous and $C_d = 24/\mathrm{Re}_d$ and for $\mathrm{Re}_d > 10^3$ the drag force is linked to the surrounding liquid inertia and $C_d \simeq 0.44$. In the present experiments, the droplet Reynolds number Re_{d0} based on the drop velocity right after breakup u_{d0} lies between 20 and 76. The drag force is thus in an intermediate regime. Indeed, the viscous effects are confined in a boundary layer around the droplet that detaches for $\mathrm{Re}_d > 20$ and form an axisymmetric and steady vortex ring behind the sphere up to $\mathrm{Re} \simeq 210$ [34]. In that range of Re_d and for large viscosity ratio between the dispersed phase and the continuous phase, which is here equal to 54, the following semiempirical law can be used [35] (Fig. S2 [36]):

$$C_d = \frac{24}{\mathrm{Re}_d} + 4\mathrm{Re}_d^{-1/3}. \tag{15}$$

As shown in Figs. 6(a) and 6(b), the integration of Eqs. (13) and (14) correctly predicts the transverse and longitudinal displacements of charged droplets. The transverse velocity $u_{d,x}$ over a longer period of time is also plotted in Fig. 6(a) inset. The droplet initially experiences a strong acceleration, then it slows down because of air drag, reaches a maximum and finally decelerates. Meanwhile, the vertical velocity $u_{d,z}$ continuously decreases [Fig. 6(b) inset], and should further reaches the terminal velocity u_t for low Reynolds number $u_t = \rho g d^2/18\eta_{\mathrm{air}}$. The origine of the x coordinate being located at the tip of the liquid jet and since the injector is placed right before the electrode, the grounded plate is thus at about $x = 9$ cm. The droplet flight time is then approximately 22 ms. The corresponding trajectory in the $\{x, y\}$ plane is shown in Fig. 6(c). Here, the impact diameter is 10 mm and varies due to fluctuations of the lateral offset of the drops x_{d0} as well as variations of λ_d linked to initial velocity fluctuations. However, to capture the whole distribution of droplets in the transverse plane and reported in Fig. 3(c), this simplified model should include three dimensional features of the spray as well as interactions with other droplets, having both electrostatic and hydrodynamic origin, but this is beyond the scope of this study. Also, one may take into account the electric field generated by the cylindrical electrode that ultimately attracts droplets since they carry an opposite electrical charge (Fig. S1 [36]). Indeed, assuming that the electric field generated between the electrode and the collecting bath or plate is oriented along z and equal to U_e/H_i, the equation of motion along z becomes

$$m_d \frac{d^2 z_d}{dt^2} = m_d g - \frac{\pi}{8}\rho_{\mathrm{air}} d^2 C_d u_d^2 \cos\alpha - \frac{q_e U_e}{H_i}. \tag{16}$$

As reported in Fig. 6(c), the integration of Eqs. (13) and (16) leads to a larger lateral spread of the droplet. This is a consequence of a higher deceleration of the droplet along the vertical direction in presence of the electric field that lets more time for the droplet to move along the transverse direction.

To avoid fragmentation when droplets enter the oil bath, the Weber number evaluated with the droplet velocity u_{di} just before the impact with the free surface, i.e., $\mathrm{We} = \rho d u_{di}^2/\gamma$, should be smaller than 40 [37]. Considering the largest velocity encountered during experiments obtained with $d = 100$ μm and $q = 60$ ml/h, the resulting impact velocity is 4.4 m/s which corresponds to a maximal impact Weber number We_i equal to 27, thus below the critical one above which droplet fragmentation can occur. We note that because of the high interfacial tension of the aqueous solution with air as compared with oil, complete wetting of water droplets by oil is energetically favorable [38]. The full engulfment of droplets in the oil bath then occurs whatever their entry velocity.

C. Polymerization

After entering into the oil bath, the polymerization is boosted thanks to diffusion of TEMED from the oil to the droplets which then turn into gel microspheres. A microscope image of a collection of gel microspheres suspended in water is shown in Fig. 7(a). Even though the size is homogeneous, we notice that a few microspheres are not perfectly spherical. Moreover, we observe the presence of a drop which exhibits a different optical contrast with the surrounding. We attribute this difference to

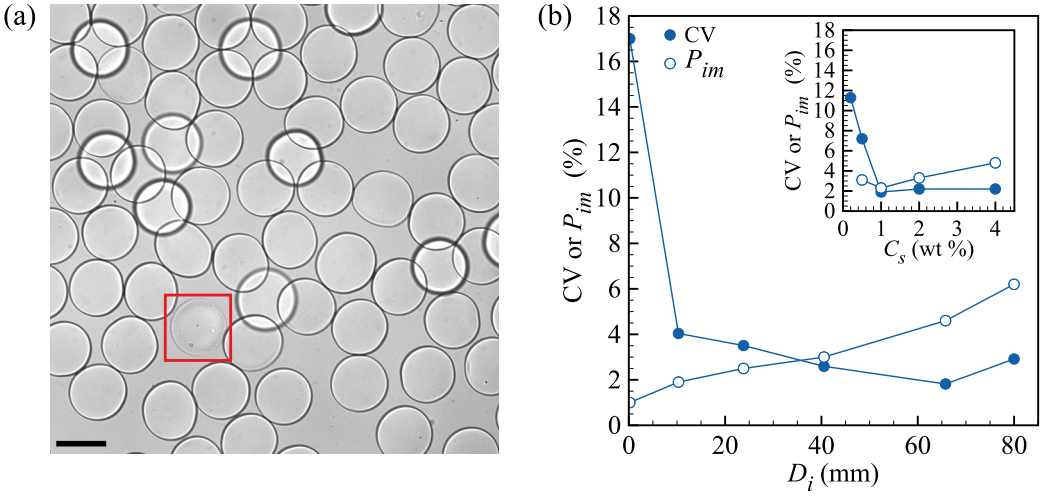

FIG. 7. (a) Snapshot of a collection of gel microspheres formed from 100 μm size acrylamide solution droplets. The red square point out a microsphere having a contrasting morphology from the others. Scale bar is 100 μm. (b) Coefficient of variation CV of the microspheres size and probability of imperfect microspheres P_{im} as a function of the impact diameter. Inset: same observables as a function of the surfactant concentration C_s in the oil. The injector diameter d_i is 40 μm, the flow rate is 30 ml/h, the frequency and amplitude of the actuation are 16 kHz and 10 V, respectively.

an imperfect polymerization of the droplet content that leads to a less dense network and thus a lower optical index. From such an image, we evaluate the proportion of imperfect gel microspheres P_{im} for various values of the electrode voltage here represented by the impact diameter D_i in Fig. 7(b). While the monodispersity level is enhanced when D_i increases, the value of P_{im} is an increasing function of D_i. This tendency is also observed when the amount of surfactant is increased [inset of Fig. 7(b)]. Since the concentration is above the critical micellar concentration, this indicates that some compounds are solubilized in oil thanks to the presence of micelles which in turn alters the polymeric network formation. We may then wonder why the resulting gel features is different among the same batch of microspheres.

Since mass transport from a droplet to the surrounding medium is a diffusive process that can be modified by convection and by the presence of neighboring droplets, we recorded the emulsification step at the level of the whole oil container. For avoiding optical deformation introduced by a cylindrical beaker, we performed the experiments with a cubic container, having thus flat walls. Snapshots at different times and diameter of the conical spray are presented in Fig. 8. The first snapshot has been taken just after the first droplets enter the oil, at a time noted t_0. The second one corresponds to the time when the first droplets arrive at the container's bottom and the third one about 12 s later. The last image shows the emulsion droplets location in the bath 5 s after the injection was turned off. Since the density of the aqueous phase ρ is larger than the oil density ρ_{oil}, the emulsion droplets will ultimately sink towards the bottom but on a timescale that depends on spray features. When droplets are not charged, the droplets form a slightly wider droplets stream [Fig. 8(a)], due to the strong deceleration of droplets [Fig. 2(c)] induced by an increase of the surrounding fluid 's viscosity as well as density leading to an added mass [39]. The corresponding transport time is less than a second and it is much smaller than the one given by motion of an isolated droplet. Indeed, for an isolated droplet the sedimentation velocity u_s is given by $u_s = (\rho - \rho_{\text{oil}})gd^2/(18\eta_{\text{oil}})$, and it is equal to 1 mm/s for 100 μm size aqueous droplet. The height H_o of the oil bath being about 38 mm, the transport time H_o/u_s is equal to 50 s. The emulsion is thus falling about 67 times faster than a single droplet. This behavior is due to the fact

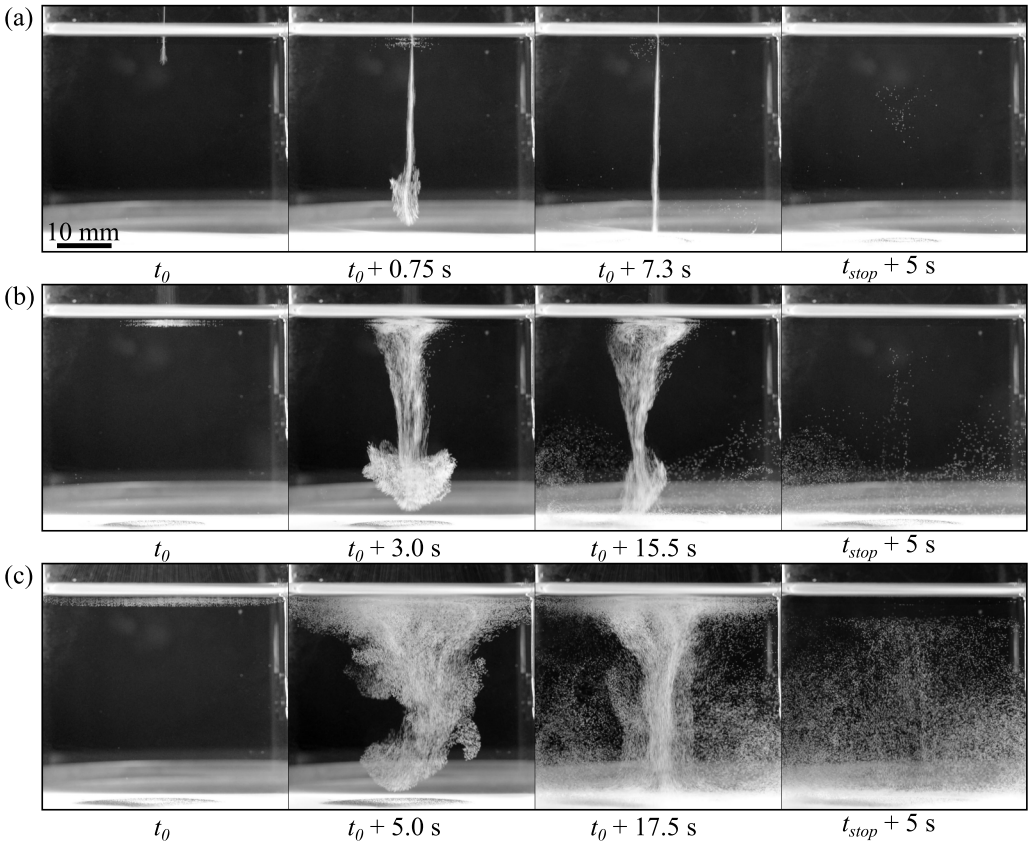

FIG. 8. Snapshots showing the flow features of the emulsion droplets in the oil bath from the initial impact, during production and 5 s after stopping the water flow. Three conditions of the impact diameters are shown, (a) $D_i = 0.25$ mm (without electric field), (b) $D_i = 5$ mm, and (c) $D_i = 50$ mm, with $d_i = 50$ µm, $q = 30$ ml/h, $f = 17$ kHz, and $U_p = 10$ V.

that the emulsion occupies solely a portion of the cross section of the container that allows the counter flow of the continuous phase to bypass the suspension of droplets thus reducing viscous dissipation. The volume of fluid containing the emulsion then behaves as a liquid whose density increases with the volume fraction ϕ of the dispersed phase like for a cloud of solid particles [40]. The sedimentation velocity is thus an increasing function ϕ, in contrast with the sedimentation of a suspension that occupies the whole cross-section of the container and where the sedimentation front is a decreasing function of ϕ [41]. The emulsion is finally spreading at the bottom of the cuvette where polymerization of the droplet content goes on.

Charging droplets induces a larger impact area and thus a lower volume fraction ϕ of the emulsion formed beneath the free surface. As a consequence, the sedimentation velocity is decreasing and the transport time is nearly multiplied by 7 for the largest spray [Fig. 8(c)]. The corresponding velocity is still relatively large even though the emulsion initially occupies the whole area of the free surface. This is a direct consequence of the spatial distribution of droplets inside the spray which are more numerous, leading to a higher ϕ, close to the center [Fig. 3(c)]. The density of the effective-fluid is thus larger in the center and triggers a vortex like flow where the droplets are entrained through the center. Most of the droplets quickly spread over the bottom but some of them are entrained by the upwards flow. The sedimentation time of droplets is thus more distributed for higher impact area. We therefore hypothesize that such mixing enhances the leakage of compounds

TABLE I. Gel microsphere size for various drop sizes and concentrations of monomers.

d (μm)	C_{Am} (vol %)	d_m (μm)	α
50	6.2	61.8	1.24
50	9.3	59.6	1.19
100	5.0	134	1.34
100	6.2	123.5	1.24
100	9.3	115.8	1.16

from the droplets, concomitant to an increase of P_{im}. Also, such a leakage should be limited when droplets form a compact emulsion by reducing the surrounding fluid volume and thus the amount of solubilized molecules.

The impact of monomers and droplet size on the features of gel microspheres, obtained at optimal conditions, is summarized in Table I. The microsphere diameter d_m, and thus the gel swelling, is increased when monomer concentration is reduced. This a signature of a less dense network along with a softer gel [42]. We also note that the swelling ratio $\alpha = d_m/d$ is similar for both droplet size. The optimal flow rate for 100 μm droplet size is 30 ml/h and is equal to 9 ml/h for 50 μm, which is substantially higher than a single droplet generator in a microfluidic system [12].

Finally, as shown in Fig. 9, a compact suspension of gel microspheres in water is able to flow through a tapered glass capillary thanks to their ability to be easily deformed. Such gel beads can thus be re-injected one by one as required for optimized encapsulation [12,43].

III. CONCLUSION

In this article, we reported a high throughput technique to create monodisperse gel microspheres that relies on suspension polymerization. Here, the emulsion droplets containing monomers are initially formed in air from a micrometer size liquid jet under controlled perturbations. This atomization step allows the use of large flow rates compared to droplet-based microfluidic techniques which is the gold standard strategy to obtain precise sizes. The main limitation arises from the merging of colliding droplets especially when they cross the free surface of the oil bath containing a catalyzer of the polymerization reaction. This is limited and even avoided by first electrically charging the droplets in air thanks to a cylindrical electrode and by adding the right amount of surfactants into the oil. A simple model that considers the electrostatic interaction between a droplet and its two closet neighboring droplet fairly recapitulates the droplet trajectory but would need further refinements to fully predict the spray features as for electrospray [44,45]. Tuning the electrode voltage, and thus the electrical charge carried by individual droplets, modify the lateral spreading of the spray

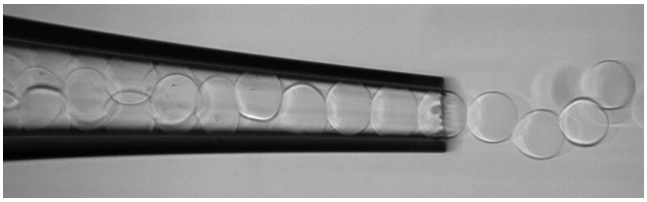

FIG. 9. Extrusion of a compact collection of 123 μm gel microspheres through a tapered glass capillary ending with a 110 μm inner diameter tip.

TABLE II. Surface and interfacial tensions γ for various couples of fluids at room temperature.

Fluid 1	Fluid 2	γ (mN/m)
NaCl solution (100 mM)	Air	71.8
Dodecane	Air	23.0
Dodecane + Span 83 (1wt%)	Air	22.6
Dodecane + Span 83 (1wt%) + TEMED (0.2 wt%)	Air	22.8
Dodecane	NaCl solution (100 mM)	44.5
Dodecane + Span 83 (1wt%)	NaCl solution (100 mM)	8.0
Dodecane + Span 83 (1wt%) + TEMED (0.2 wt%)	NaCl solution (100 mM)	2.8

where droplet location is more probable at the spray's center set by the liquid jet. This heterogenous spatial distribution then sets a critical flow rate, or flux of droplets, above which collision between droplets and thus coalescence cannot be avoided. Another limitation to obtain homogeneous gel microspheres is linked to the inverse suspension polymerization process itself. Indeed, since the system is composed of two liquids with surfactants, the partition of chemical compounds between the phases is usually encountered and may affect the polymerization step. This is the case in the present study. We managed to minor gel feature heterogeneity between gel beads by minimizing the transport time of droplets from the oil bath free surface to the bottom of the container. We show that the motion of droplets inside the oil bath is linked to the spray features. We hypothesize that the compact emulsion collected at the bottom of the container limits exchange between the dispersed phase and the continuous one.

The methodology reported in the article allows the production of well calibrated gel microspheres at a high throughput while preventing a direct contact between reactants during the droplet formation step as well as the use of nonfluorinated oil as usually used in microfluidic context. Also, this process has been developed for polyacrylamide gel but we believe that it is a versatile strategy to produce polymeric networks composed of other building blocks and further investigations are ongoing.

IV. MATERIAL AND METHODS

A. Chemicals and fluid properties

The following compounds were used to produce gel microspheres: acrylamide (Am) solution at 40% (v/v) (Sigma-Aldrich, suitable for electrophoresis), N,N'-Methylenebisacrylamide (MBAm) solution at 2% (v/v) (Sigma-Aldrich, suitable for electrophoresis), tetramethylethylenediamine (TEMED) (Millipore, for synthesis), ammonium persulfate (APS) (Sigma-Aldrich, molecular biology grade), phosphate-buffered saline (PBS, 1x) (Sigma-Aldrich, suitable for cell culture), sodium chloride (NaCl) (Sigma-Aldrich), n-dodecane (Sigma-Aldrich, synthesis grade), sorbitan sesquioleate (Span 83) (Sigma-Aldrich), sodium dodecyl sulfate (SDS) (Sigma-Aldrich).

The density of dodecane ρ_{oil} is 750 kg/m^3 and its dynamic viscosity η_{oil} is 1.5 mPa.s at 20°C [46]. The surface and interfacial tensions γ for various couples of fluids, measured by the pending drop technique (SA100, Krüss) at room temperature, are reported in Table II

The critical micellar concentration (CMC) of Span 83 in dodecane is 0.2 mM [47], corresponding to a concentration of 0.016 wt%. All experiments have been done with concentrations above CMC.

B. Experimental setup

Fluid flow is managed with the help of a syringe pump (Nemesys, Cetoni) by using a glass syringe equipped with a syringe filter having a 0.45 µm mesh size. A liquid jet is formed with an injector equipped with a piezoelectric element (MJ-ABP-01, MicroFab Technologies) having an

exit diameter of 25 μm, 40 μm, or 50 μm. An arbitrary waveform generator (TG1010, TTi) is used to impose a sinusoidal voltage to the piezoelectric element with an amplitude U_p and a frequency f. The syringe is connected to the injector with 0.8 mm inner diameter teflon tube. The injector is fixed to a 3D printed homemade holder together with a coaxial cylindrical electrode. The length of the electrode is 10 mm and its internal diameter is 16 mm. A DC power supply coupled to a $\times 1000$ amplifier (623B, Trek) is used to set the electrical voltage U_e to the electrode. The droplets are collected in oil contained in a cylindrical glass beaker having a diameter of 8 cm. The oil bath is grounded since otherwise droplets are repulsed by the accumulated electric charges and do not enter into the bath anymore. The wall of the container is made hydrophobic by silanization to prevent droplets to wet the wall. The injector and electrode holder and the collecting oil bath are enclosed in a plexiglass box to ensure user safety when using monomer solutions and also to prevent any external flow disturbances of the fine spray. A manual shutter between the injector and the oil bath is used to allow for stable spray formation before collecting aqueous droplets in oil. The shutter is composed of a cup with a diameter of 10 cm attached to a vertical rod which can rotated in the horizontal plane from the outside the box (see movie S1 [36]).

C. Visualization and image analysis

The fragmentation of liquid jets is visualized with a high speed camera (FastCam SA3, Photron) mounted on a macro zoom microscope (MVX10, Olympus) set horizontally. The jet is back-illuminated with a LED panel (SLLUB backlight, Phlox). This illumination is not powerful enough to capture the dynamics of jet fragmentation for the range of experimental frequencies, up to 40 kHz. The frame rate is thus reduced down to a 1 kHz with adding a few Hz to captured around 10 images of a whole period, namely by stroboscopic effect. Destabilization of the stream of charged droplets is imaged at 4 kHz. Droplet trajectory is then achieved with an image processing program developed with MATLAB. The spray shape is obtained from snapshots taken with a still camera (Nikon). The distribution of droplet location in the transverse plane of the spray is measured by collecting droplets containing carbon black on a piece of paper during about 3 s. The impact pattern, scanned at 600 dpi, is then analyzed with a program developed with MATLAB. The images are first binarized and the center of mass is determined. Then, the probability P_d to find a droplet at a distance r is evaluated by counting the number of black N_b and white N_w pixels in a ring having a width of 20 pixels, about 85 μm, i.e., $P_d = N_b/(N_b + N_w)$.

D. Gel microspheres synthesis

The composition of the monomers solution gel synthesis is inspired from the work of Klein and coworkers [12]. Aqueous solutions are prepared with ultra-pure water (Milli-Q). While the amount of acrylamide varies, the ratio between Am and MBAm is kept constant and equal to 0.03. The solution contains 0.45% (w/v) APS and 40% (v/v) PBS. PBS was used for further applications involving the encapsulation of biomolecules. For experiments without monomers, a 100 mM NaCl solution is utilized. The monomers solution is degassed in a vacuum chamber set at a pressure of 900 mbar during 15 min, while simultaneously stirring the solution with a magnetic stirrer. APS, from a 10 wt% solution, is added after the degassing step and mixed with the help of a micropipette by several forward and reverse pipetting. The oil contains 0.2% (v/v) TEMED and various concentrations of Span 83 and it is also degassed with the same procedure.

A volume of 1 ml of the monomers solution is sprayed and collected in the oil bath at rest. Then, after the last droplets sediment at the bottom of the beaker, the oil excess is removed and 10 ml are left. Reaction at room temperature lasts 3 h. The suspension is then transferred in 15 ml Falcon tube. After gel beads sedimentation, the supernatant is removed and replaced by 12 ml of 2 wt% SDS solution. The tube is shaken by hand for 10 s and centrifuged to removed the supernatant containing oil. This operation is done a second time.

ACKNOWLEDGMENTS

This work has received the support of "Institut Pierre-Gilles de Gennes" (laboratoire d'excellence, "Investissements d'avenir" program ANR-10-IDEX-0001-02 PSL and ANR-10-LABX-31 and was supported by a public grant overseen by the French National Research Agency (ANR), Project Reference No. ANR19-CE06-0026 (ElectroFluid). We thank HiFiBio Therapeutics for funding as well as Sami Ellouze and Yannick Pousse for fruitful discussions on bead polymerization.

[1] Y. S. Zhang and A. Khademhosseini, Advances in engineering hydrogels, Science **356**, eaaf3627 (2017).
[2] R. Ajdary, B. L. Tardy, B. D. Mattos, L. Bai, and O. J. Rojas, Plant nanomaterials and inspiration from nature: Water interactions and hierarchically structured hydrogels, Adv. Mater. **33**, 2001085 (2021).
[3] N. A. Peppas, J. Z. Hilt, A. Khademhosseini, and R. Langer, Hydrogels in biology and medicine: From molecular principles to bionanotechnology, Adv. Mater. **18**, 1345 (2006).
[4] J. L. Drury and D. J. Mooney, Hydrogels for tissue engineering: Scaffold design variables and applications, Biomaterials **24**, 4337 (2003).
[5] T. R. Hoare and D. S. Kohane, Hydrogels in drug delivery: Progress and challenges, Polymer **49**, 1993 (2008).
[6] X. Liu, J. Liu, S. Lin, and X. Zhao, Hydrogel machines, Mater. Today **36**, 102 (2020).
[7] W. Zhang, P. Feng, J. Chen, Z. Sun, and B. Zhao, Electrically conductive hydrogels for flexible energy storage systems, Prog. Polym. Sci. **88**, 220 (2019).
[8] E. A. Appel, J. del Barrio, X. J. Loh, and O. A. Scherman, Supramolecular polymeric hydrogels, Chem. Soc. Rev. **41**, 6195 (2012).
[9] M. J. Webber, E. A. Appel, E. W. Meijer, and R. Langer, Supramolecular biomaterials, Nat. Mater. **15**, 13 (2016).
[10] A. C. Daly, L. Riley, T. Segura, and J. A. Burdick, Hydrogel microparticles for biomedical applications, Nat. Rev. Mater. **5**, 20 (2020).
[11] B. M. Tiemeijer and J. Tel, Hydrogels for single-cell microgel production: Recent advances and applications, Front. Bioeng. Biotechnol. **10**, 891461 (2022).
[12] A. M. Klein, L. Mazutis, I. Akartuna, N. Tallapragada, A. Veres, V. Li, L. Peshkin, D. A. Weitz, and M. W. Kirschner, Droplet barcoding for single-cell transcriptomics applied to embryonic stem cells, Cell **161**, 1187 (2015).
[13] S. Girardo, N. Träber, K. Wagner, G. Cojoc, C. Herold, R. Goswami, R. Schlüßler, S. Abuhattum, A. Taubenberger, F. Reichel, D. Mokbel, M. Herbig, M. Schürmann, P. Müller, T. Heida, A. Jacobi, E. Ulbricht, J. Thiele, C. Werner, and J. Guck, Standardized microgel beads as elastic cell mechanical probes, J. Mater. Chem. B **6**, 6245 (2018).
[14] Y. Shen, B. Zhang, Z. Yi, L. Zhang, J. Ling, S. Wang, Z. Sun, M. Z. Iqbal, and X. Kong, Microfluidic fabrication of x-ray-visible sodium hyaluronate microspheres for embolization, RSC Adv. **13**, 20512 (2023).
[15] B. Brooks, Suspension polymerization processes, Chem. Eng. Technol. **33**, 1737 (2010).
[16] G. T. Vladisavljevic, I. Kobayashi, and M. Nakajima, Production of uniform droplets using membrane, microchannel and microfluidic emulsification devices, Microfluid. Nanofluid. **13**, 151 (2012).
[17] P. Zhu and L. Wang, Passive and active droplet generation with microfluidics: A review, Lab Chip **17**, 34 (2017).
[18] W. Li, L. Zhang, X. Ge, B. Xu, W. Zhang, L. Qu, C.-H. Choi, J. Xu, A. Zhang, H. Lee, and D. A. Weitz, Microfluidic fabrication of microparticles for biomedical applications, Chem. Soc. Rev. **47**, 5646 (2018).
[19] Z. Zhao, Z. Wang, G. Li, Z. Cai, J. Wu, L. Wang, L. Deng, M. Cai, and W. Cui, Injectable microfluidic hydrogel microspheres for cell and drug delivery, Adv. Funct. Mater. **31**, 2103339 (2021).

[20] J. Eggers and E. Villermaux, Physics of liquid jets, Rep. Prog. Phys. **71**, 036601 (2008).
[21] C. Clanet and J. C. Lasheras, Transition from dripping to jetting, J. Fluid Mech. **383**, 307 (1999).
[22] J. Eggers, Nonlinear dynamics and breakup of free-surface flows, Rev. Mod. Phys. **69**, 865 (1997).
[23] S. Middleman and J. Gavis, Expansion and contraction of capillary jets of newtonian liquids, Phys. Fluids **4**, 355 (1961).
[24] A. Sevilla, The effect of viscous relaxation on the spatiotemporal stability of capillary jets, J. Fluid Mech. **684**, 204 (2011).
[25] D. B. Harmon, Jr., Drop sizes from low speed jets, J. Franklin Inst. **259**, 519 (1955).
[26] P. Vassallo and N. Ashgriz, Satellite formation and merging in liquid jet breakup, Proc. R. Soc. Lond. A **433**, 269 (1991).
[27] K. C. Chaudhary and T. Maxworthy, The nonlinear capillary instability of a liquid jet. Part 3. Experiments on satellite drop formation and control, J. Fluid Mech. **96**, 287 (1980).
[28] J. M. Schneider, N. R. Lindblad, C. D. Hendricks, Jr., and J. M. Crowley, Stability of an electrified liquid jet, J. Appl. Phys. **38**, 2599 (1967).
[29] H. Brandenberger, D. Nüssli, V. Piëch, and F. Widmer, Monodisperse particle production: A method to prevent drop coalescence using electrostatic forces, J. Electrostat. **45**, 227 (1999).
[30] H. Domejean, M. de la Motte Saint Pierre, A. Funfak, N. Atrux-Tallau, K. Alessandri, P. Nassoy, J. Bibette, and N. Bremond, Controlled production of sub-millimeter liquid core hydrogel capsules for parallelized 3D cell culture, Lab Chip **17**, 110 (2017).
[31] L. She, Y. Fang, L. Hu, R. Su, and X. Fu, Mitigating jitter in droplet stream by uniform charging, Phys. Fluids **34**, 111704 (2022).
[32] J. M. Crowley, Lateral instability of a stream of charged droplets, Phys. Fluids **11**, 1372 (1968).
[33] O. M. Ondimu, V. A. Ganesan, M. J. Gatari, J. C. M. Marijnissen, and L. L. F. Agostinho, Modeling simple-jet mode electrohydrodynamic-atomization droplets' trajectories and spray pattern for a single nozzle system, J. Electrostat. **89**, 77 (2017).
[34] T. A. Johnson and V. C. Patel, Flow past a sphere up to a Reynolds number of 300, J. Fluid Mech. **378**, 19 (1999).
[35] V. Y. Rivkind and G. M. Ryskin, Flow structure in motion of a spherical drop in a fluid medium at intermediate Reynolds numbers, Fluid Dyn. **11**, 5 (1976).
[36] See Supplemental Material at http://link.aps.org/supplemental/10.1103/PhysRevFluids.9.083604 for a series of long time exposure snapshots of the conical spray at various electrode voltages, values of drag coefficients obtained from experiments and numerical simulations and compared to Eq. (15), movie showing the atomization of an aqueous solution collected in an oil bath, which includes Ref. [48].
[37] H. Lhuissier, C. Sun, A. Prosperetti, and D. Lohse, Drop fragmentation at impact onto a bath of an immiscible liquid, Phys. Rev. Lett. **110**, 264503 (2013).
[38] S. Torza and S. Mason, Three-phase interactions in shear and electrical fields, J. Colloid Interface Sci. **33**, 67 (1970).
[39] J. M. Aristoff, T. T. Truscott, A. H. Techet, and J. W. M. Bush, The water entry of decelerating spheres, Phys. Fluids **22**, 032102 (2010).
[40] B. Metzger, M. Nicolas, and É. Guazzelli, Falling clouds of particles in viscous fluids, J. Fluid Mech. **580**, 283 (2007).
[41] J. F. Richardson and W. N. Zaki, The sedimentation of a suspension of uniform spheres under conditions of viscous flow, Chem. Eng. Sci. **3**, 65 (1954).
[42] M. Quesada-Pérez, J. Maroto-Centeno, J. Forcada, and R. Hidalgo-Alvarez, Gel swelling theories: The classical formalism and recent approaches, Soft Matter **7**, 10536 (2011).
[43] A. R. Abate, C.-H. Chen, J. J. Agresti, and D. A. Weitz, Beating poisson encapsulation statistics using close-packed ordering, Lab Chip **9**, 2628 (2009).
[44] A. M. Gañán-Calvo, J. C. Lasheras, J. Dávila, and A. Barrero, The electrostatic spray emitted from an electrified conical meniscus, J. Aerosol Sci. **25**, 1121 (1994).
[45] J. Rosell-Llompart, J. Grifoll, and I. G. Loscertales, Electrosprays in the cone-jet mode: From taylor cone formation to spray development, J. Aerosol Sci. **125**, 2 (2018).

[46] D. Ducoulombier, H. Zhou, C. Boned, J. Peyrelasse, H. Saint-Guirons, and P. Xans, Pressure (1-1000 bars) and temperature (20-100.degree.c) dependence of the viscosity of liquid hydrocarbons, J. Phys. Chem. **90**, 1692 (1986).

[47] J. Jiao and D. J. Burgess, Ostwald ripening of water-in-hydrocarbon emulsions, J. Colloid Interface Sci. **264**, 509 (2003).

[48] F. W. Roos and W. W. Wollmarth, Some experimental results on sphere and disk drag, AIAA J. **9**, 285 (1971).